Another measure to compare the time series of wind speeds is the rmse as defined in equation 7. Figures 36 and 37 show the rmse for both downscaling methods compared to the COSMO-EU wind speeds. The rmse maps show similar patterns for the statistical downscaling at 50 m and 140 m heights with rmse being smallest in flat onshore terrain and higher in the offshore regions and in the mountaneous regions. This is true for both heights, however rmse values are almost everywhere higher at 140 m height. This is an expected result since the rms is a homogenous function of first degree
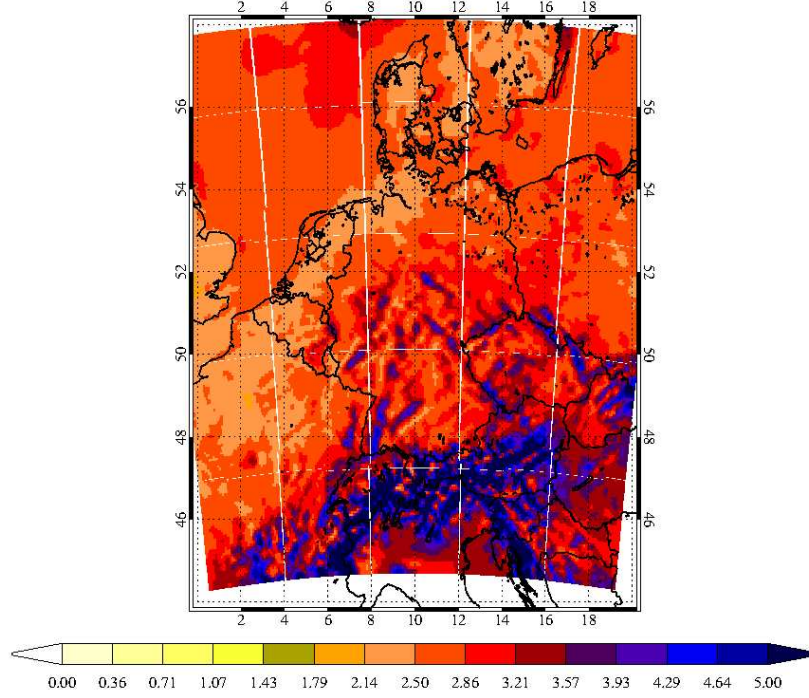

Figure 37: Rmse for the investigated domain per grid cell for February until November 2009 between COSMO-EU wind speeds and dynamically downscaled wind speeds at 140 m height.

$$\mathrm{rms}(\alpha \cdot v) = \alpha \cdot \mathrm{rms}(v), \alpha \in R.$$

Besides the wind speeds also the generated feed-in for Germany from February until November 2009 was compared. Feed-in was calculated with the Enercon E-126 power curve at a hub height of 140 m for Germany with the capacity distribution within Germany as described in section ??. The results can be seen in tables 9 and 10. The higher wind speeds that were observed for the dynamically downscaled wind speeds directly lead to a higher overall feed-in. While dynamically downscaled wind speeds in

the whole domain are roughly 20% higher than statistically downscaled and COSMO-EU wind speeds the feed-in for Germany is roughly 40% higher compared to the calculations for the statistically downscaled and COSMO-EU wind speeds with also a 25% higher standard deviation of hourly capacity factors.

	Dyn. Downscaling	COSMO-EU	Stat. Downscaling
Feed-in [TWh]	121.6	88.8	85.6
Mean [%]	30.7	22.4	21.7
Stdev [%]	25.1	20.6	20.2

Table 9: Feed-in for Germany for February until November 2009 calculated with the Enercon E-126 power curve from the three different wind speed models at 140 m hub height. Mean and Standard deviation are for hourly capacity factors.

	Dyn & COSMO	Stat & Cosmo	Dyn & Stat
Correlation	0.908	0.913	0.889

Table 10: Correlation coefficients between the hourly feed-in time series' calculated from the three different wind speed models for Germany with the Enercon E-126 power curve at 140 m hub height for February until November 2009.

In addition the correlation coefficients for the feed-in time series were pairwise computed. It can be seen in table 10 that the correlation coefficients are very similar around 0.91 between the COSMO-EU feed-in and feed-in from statistically downscaled wind speeds respectively dynamically downscaled wind speeds.

3.5.   Dependency of the feed-in from wind on hub height and power curve

One specific wind power curve and hub height was chosen to simulate feed-in from wind for the Restore 2050 project. The feed-in was calculated using the Enercon E-126 power curve modified with 5% plain losses at 140 m hub height. This section analyses the effect of different hub heights and power curves on the resulting feed-in. The planetary boundary layer is the lowest part of the atmosphere whose behaviour is influenced by the contact to the planetary surface. In the layer surface friction slows the wind while well above the Earth's surface the flow is almost frictionless.
Conclusively, wind speeds and wind power increase with height above the ground in dependency of the surface roughness (Fig. 38). The figure shows the weekly capacity factor for hub heights of 100, 140 and 180 m computed with the Enercon E-126 power curve for Germany in the year 2012. Increasing hub heights lead to increased capacity factors due to higher wind speeds. Increasing hub height from 100 m to 180 m leads to around 50% of increase in power output over the year. The weekly capacity factors was also calculated for the Enercon E-126 and the average of the Enercon E-82/Vestas
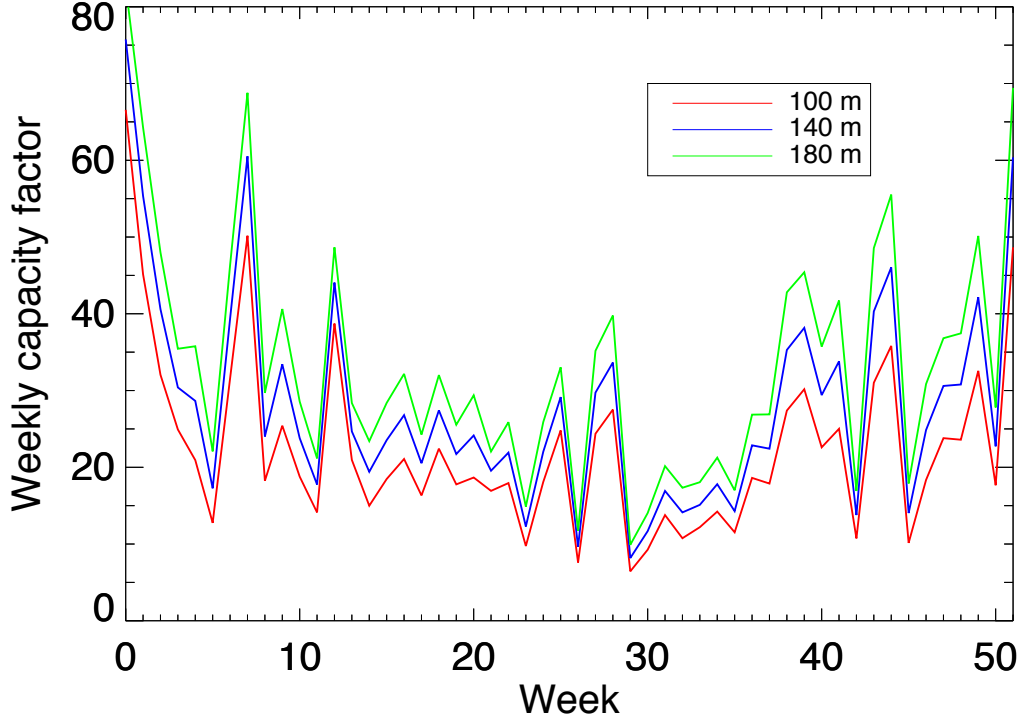
Figure 38: Weekly capacity factor [%] for wind computed applying the Enercon E-126 power curve to COSMO-EU wind speeds in the year 2012 for three different hub heights for Germany.

V-90 power curve (Fig. 39). Again on the weekly base there is an almost linear scaling between the two powercurves. The Enercon E-126 has a hub height of 135 m and a nameplate capacity of 7,5 MW. This causes it to reach the nameplace capacity as power output only at high wind speeds. Thus, it has a comparabibly low capacity factor.. Computed capacity factors for the Enercon E-82 and Vestas V-90 average are ca. 50% higher than for the Enercon E-126, while the temporal pattern is very similar.

Another possible way to investigate the influence of the power curves on the resulting feed-in is the correlation coefficient as defined in equation 8. It is a measure of a strength of a linear relationship between two variables that fulfils

$$r(v, \beta \cdot v) = r(\beta \cdot v, v) = 1,$$

with $v \in R^n, \beta \in (0, \infty)$ so a correlation factor of one implies that multiplication with a constant factor can transform two variables into each other. Figures 40 and 41 show the correlation factors between the hourly feed-in time series for wind onshore and offshore for all investigated countries in 140 m hub height. For each country one
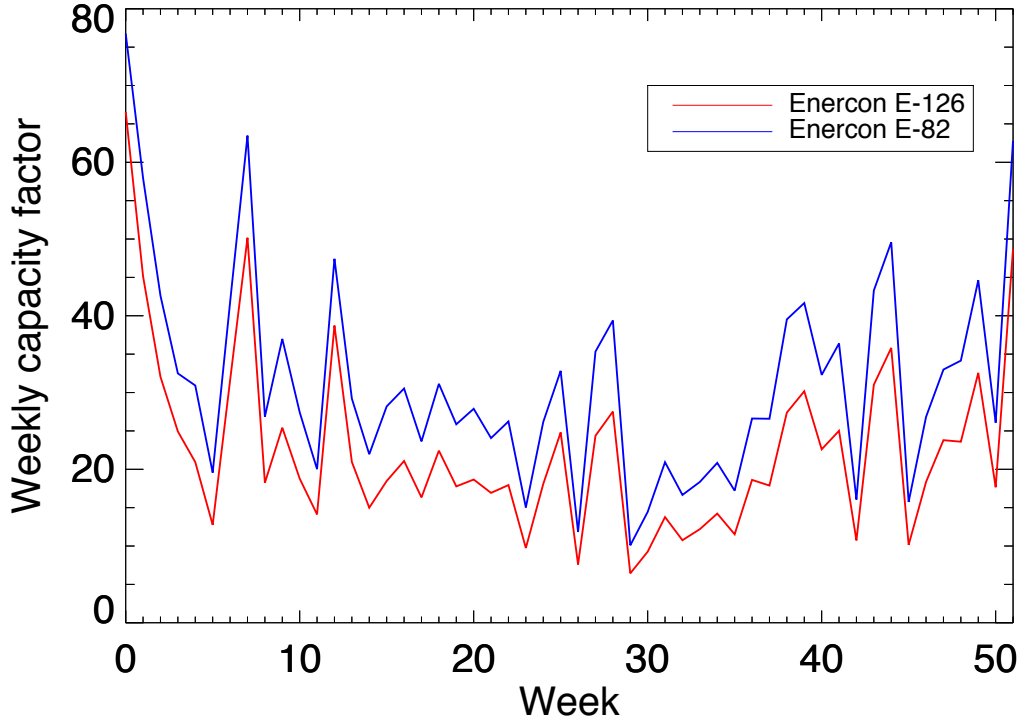
Figure 39: Weekly capacity factor[%] for wind computed using COSMO-EU wind speeds for the year 2012 for two different power curves at 100 m hub height. The red feed-in was computed for an Enercon E-126 power curve and the blue line for the average of the Enercon E-82 and the Vestas V-90 power curve.

time series was computed with the Enercon E-126 power curve and the other one was computed with one half the Enercon E-82 and the Vestas V-90 power curve (See section 2.3.1.1 for details). Oneshore the correlation factors are between 0.97 for Malta and 0.995 for Romania. The factors are lowest for small countries with high capacity factors like Malta, Denmark, the Netherlands and Ireland. Average wind speeds in these countries are in the range of $8 - 10$ m/s so in the region where differences between the two power curves are comparably large, while in South-Eastern Europe average wind speeds are around 5 m/s in 140 m height. Offshore correlation coefficients are a little bit lower ranging from 0.96 for Lithuania to 0.99 for Italy. Again Belgium and the Netherlands have rather small correlation coefficients while in South-Eastern Europe they are larger. This confirms the assumption that a linear scaling between feed-in computed on a large spatially aggregated area such as countries as they were investigated from different power curves is possible and yields reliable results. Therefore it is sufficient to compute feed-in by usage of a single power curve for wind power feed-in alone.
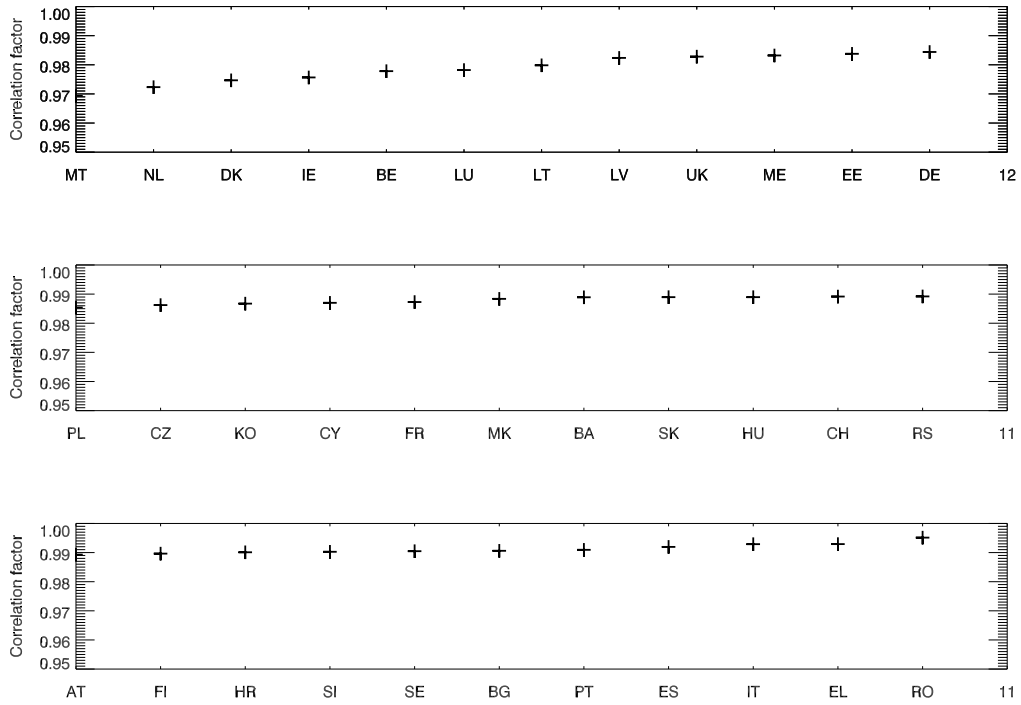
Figure 40: Correlation factors for every country investigated onshore between the time series computed with the Enercon E-126 power curve and one half the Enercon E-82 and Vestas V90 power curve for the year 2012 from COSMO-EU wind speeds in 140 m height.
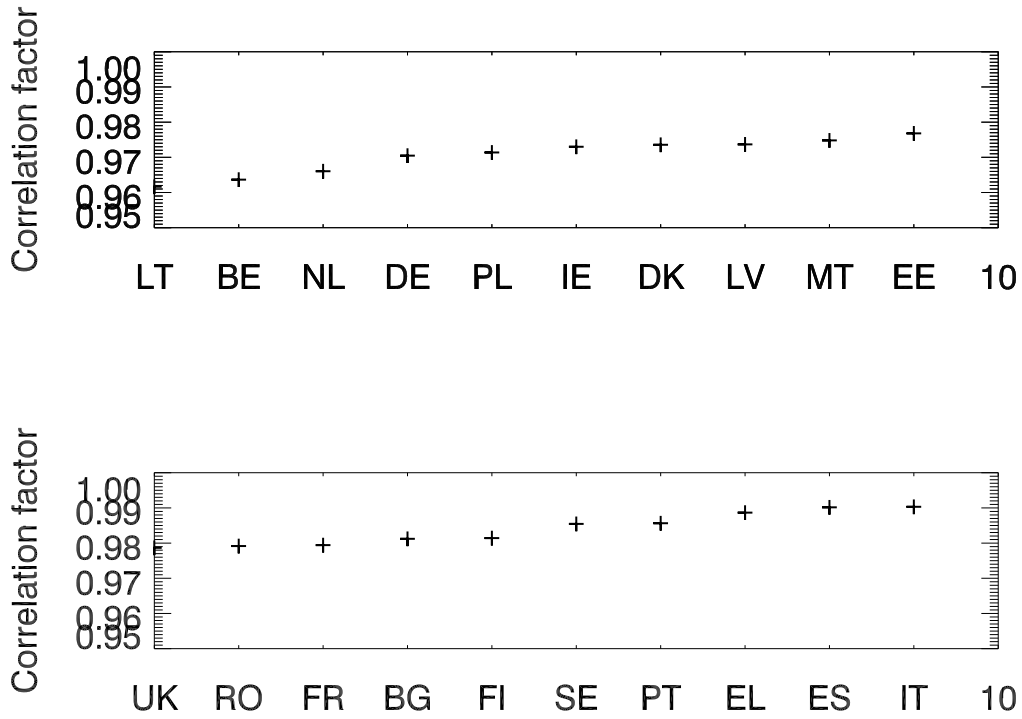
Figure 41: Correlation factors for every country investigated offshore between the time series computed with the Enercon E-126 power curve and one half the Enercon E-82 and Vestas V90 power curve for the year 2012 from COSMO-EU wind speeds in 140 m height.

4.   Summary and outlook

Restore 2050 investigates the equirements for cross-country grid extensions, usage of storage technologies and capacities, the development of new balancing technologies and the conceptual design of the future energy market which is suitable for high shares of solar and wind. To investigate these questions detailled data on renewable power production is necessary. For this purpose a highly temporally and spatially resolved weather data base covering ten years from 2003 to 2012 has been produced. The temporal resolution is one hour while the spatial resolution is 7×7 km. This report is summarizing the calculation methods from the raw data description to the power calculation methods. As far as possible data from the underlying meta studies has been used to calculate feed-in from renewable sources as described in this report. Since only capacities on the country level are given, in-country capacity distributions were modelled according to a empirically derived approach. This approach assumes that the resource dependency (wind speeds and global irradiance) of the installed capacities can be assumed to be somewhat similar for all investigated countries. Wind speed was modelled then using the power curve of an Enercon E-126 turbine for 140 m wind speeds which is almost equivalent to the hub height of the Enercon E-126 power curve of around 135 m. In addition to the description of how the feed-in was simulated some verification and investigation results were shown.

In section 3.4 the statistically downscaled wind speeds were compared with dynamically downscaled wind speeds from a WRF (Weather Research and Forecasting model). The results of the statistically downscaled model turned out to be very close in comparison to the targetted COSMO-EU wind speed at average and standard deviation as well as by measures of correlation factor of the wind speeds and the resulting feed-in. Standard deviation was slightly less for the statistically downscaled wind speeds compared to the COSMO-EU wind speeds which is expected for regression based downscaling models.

In section 3.5 the the feed-in was compared for different hub heights and two different power curves. It was shown, that on the weekly scale the capacity factors of week in between different power curves and hub heights scale almost linearly. Higher hub heights lead to higher capacity factors a change from 100 m to 180 m lead for the feed-in calculated for Germany to an increase in output of around 50%. Single-country feed-in time series computed with two different power curves were shown to have very high correlation coefficients of above 0.96 for all countries investigated onshore and offshore indicating that the usage of a single power curve to compute feed-in yields reliable results.

A. Appendix

A.1. Application of Kolmogorov-Smirnov integral

Kolmogorov-Smirnov Integral (KSI) is a popular statistical measure that serves as a measure of goodness of fit by comparing the cumulative distribution functions of two samples. It provides information on how closely the samples follow each other. In the first step, the cumulated distribution functions of the samples are drawn. Next, the supremum of a set of distances is computed for each data point, figure 42.

$$D_n = \sup_x |F_{n_2}(x) - F_{n_1}(x)|$$

where n is the number of data points and F_n is the empirical distribution function.
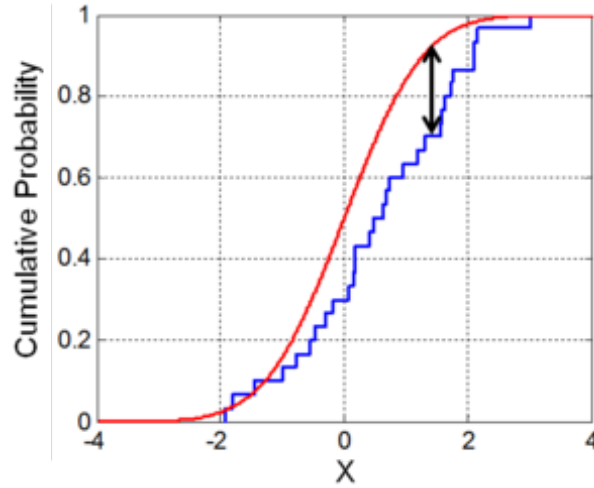

Figure 42: Illustration of Kolmogorov-Smirnov statistics

Evidently, a lower value of D_n suggests a closer proximity of the samples and vice versa. For our analysis, the KSI is computed for the reference time-series and each individual year and the lowest KSI value suggests the year with the highest capability of being the representative year.

A.2. Hypothesis test

We have applied a statistical hypothesis test to finalise the representative year from the ten years. This hypothesis test is known as the Kolmogorov-Smornov hypothesis test. It is an extension over the statistical measure of Kolmogov-Smirnov Integral discussed earlier. In the first step, a critical value (D_a) of the test statistics is chosen such that the probability of the supremum distance between the two samples be

$$p = P(D_n > D_a)$$

. So, a band width of $\pm D_a$ around the empirical distribution function $F_n(x)$ which entirely contain the distribution will have the probability of $1 - p$. In the next step, one can use a pre-defined confidence interval α (in this case 95%) to determine if the samples are drawn from the same distribution or not. Based on the definition of the null hypothesis (i.e, both the samples are drawn from the same distribution), the following decision is made from the hypothesis testing:

$$decision = \begin{cases} retain \ null \ hypothesis & \text{if } p < \alpha \\ reject \ null \ hypothesis & \text{otherwise} \end{cases}$$

For our analysis, low p values indicate that the samples are taken from the same distribution, that is, the sample can potentially reproduce the characteristics of the reference time-series and is suitable to be the representative year. The test is performed on normalised power generation of each technology and at each temporal resolution. Night time values are filtered out for solar renewables.

A.3. Concentrated Solar Power (CSP) in North Africa

It is anticipated that in 2050, solar energy import from North Africa can have significant impact on European power system. North Africa is ideally suited for installing CSP plants due to high availability of solar irradiance throughout the year. Additionally, the presence of Sahara desert strongly reduces cloud formation, thus significantly enhancing the incoming direct normal irradiance (DNI), the component which governs CSP performance. The model domain for the project RESTORE-2050 is extended to North Africa and the CSP time-series for the ten years of simulation (2003-2012) are computed. There are some inherent differences in the CSP model applied for Europe and North Africa. These differences will be discussed in the following section.

A.3.1. Data set for North Africa

A.3.1.1 Meteorological data

Similar to the European countries, the irradiance for North Africa is retrieved from Meteosat satellite images. The first two years of simulation (2003-2004) are derived from the visible channel of Meteosat First Generation (MFG) satellites with spectral range of $0.5 - 0.9\mu m$. It has a spatial resolution of 2.5×2.5 km and a temporal resolution of 30 minutes. The rest of the years are simulated with Meteosat Second Generation (MSG) satellites. To simulate the European domain, we used the high resolution visible (HRV) channel of MSG. However, this broadband channel of MSG (channel 12) has only partial coverage over North Africa. So, we used the narrowband visible channel of MSG to retrieve irradiance over North Africa. Our selected channel (VIS008) has a spectral coverage of $0.74 - 0.88\mu m$. This channel is able to supply satellite images of the hemisphere at 3×3 km spatial and 15 minutes of temporal resolutions. For uniformity, this satellite derieved irradiance is interpolated to a coarser grid of $0.5° \times 0.5°$ over North Africa for all simulated years. The temporal resolution has been maintained to 1 hour as used for the European domain.

A.3.1.2 CSP capacity

The energy [r]evolution scenario of meta-study EREC ([9]) projects a total capacity of 81 GW CSP for Europe in 2050. We assume the same CSP capacity in North Africa due to the high availability of adequate resources. According to DLR (German Aerospace Center) [21], a technical threshold of $1800 kWh/m^2/y$ annual DNI to convert solar energy to electrical energy for the mediterranean countries is assumed. This DLR report [21] also indicated an economic threshold of $2000 kWh/m^2/y$ annual DNI. The abundant irradiance over North Africa makes it possible to ensure average annual DNI to exceed these threshold values. Hence, instead of a resource-dependent distribution (as used for CSP simulation over the European domain), a homogeneous distribution of CSP plants is applied for North Africa. Since CSP is more a centralized rather than a distributed technology, a homogeneous distribution over a reduced spatial resolution of $0.5° × 0.5°$ is reasonable.

A.3.2. Cloud index data base

For North Africa a new cloud index data base is set up for the project RESTORE-2050. For European countries, however, the data was available from other projects. The set up of the new cloud index data base includes quality control of the images and an adaptation of the model to better account for anisotropic reflectivity in spring and autumn which is found to be necessary when using the narrowband channel. Since the selected channel from MFG is less sensitive to the anisotropic reflectivity and an atmospheric correction term was included in the algorithm for MFG, the results derived from MFG were free from these effects. Hence, our preliminary as well as the revised results from MSG were compared with that from MFG for 2005 which is an overlapping year between MFG and MSG satellites.

A.3.2.1 Quality control

For an enhanced quality of the time-series, satellite images with unusual artefacts (e.g., data loss at specific image segment, data loss along image pixels, recurring unusual patterns in images, images shifted to a few pixels etc.) were detected and removed. The result is shown in Fig.43 which indicates significant improvement of the quality of the data.

A.3.2.2 Removing the effects of anisotropic reflection

We observed rapid changes in ground reflectivities when using the narrow band channel. Usually, ground albedo is calculated for each time slot (quarter hourly) over a complete month. For this, it is assumed that the changes in solar elevations are small enough that the impact of anisotropic reflection is small. However, during Spring and Fall seasons, solar elevation changes rapidly and hence, calculating ground albedo over 30 days may be inappropriate. In order to overcome this, ground albedo for Spring and Fall seasons was recalculated using periods of 10 days (instead of 30). This removed the reduced
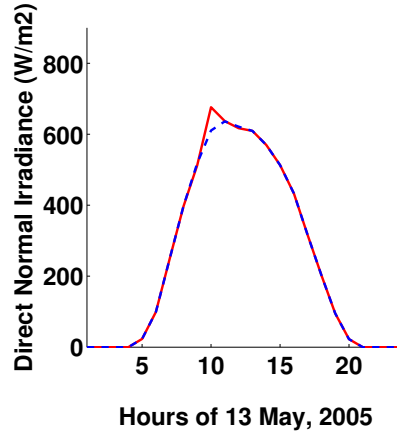
Figure 43: Diurnal cycles of DNI using respective algorithms for MFG and MSG for an example day in 2005 averaged over the entire model domain of North Africa. The figure shows improvements achieved upon quality control of satellite images.
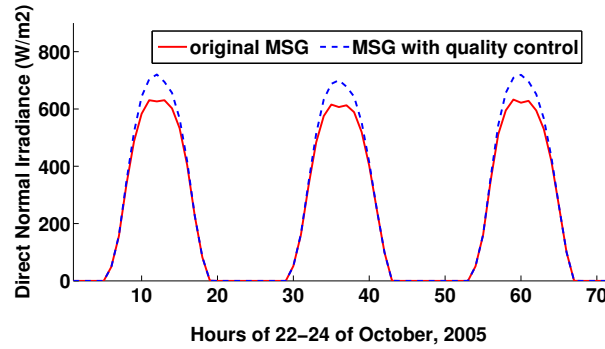

Figure 44: Diurnal cycles of DNI using respective algorithms for MFG and MSG for a few days in 2005 averaged over the model domain of North Africa. The figure represents the result of model adaptation to be more suitable to the narrowband channel.

irradiances noted around noon time of these seasons (Fig.44) and further improved the results.

The improvements are shown in Fig.45 (left) where the correlation coefficient has slightly increased for the hourly time-series. Inclusion of an atmospheric correction term in the MSG algorithm in future may further reduce the scatter and improve the correlation. Since, major modifications (including ground albedo recalculation) were restricted to Spring and Fall time only, the main differences in time-series occur during these seasons (Fig.45 (right)).
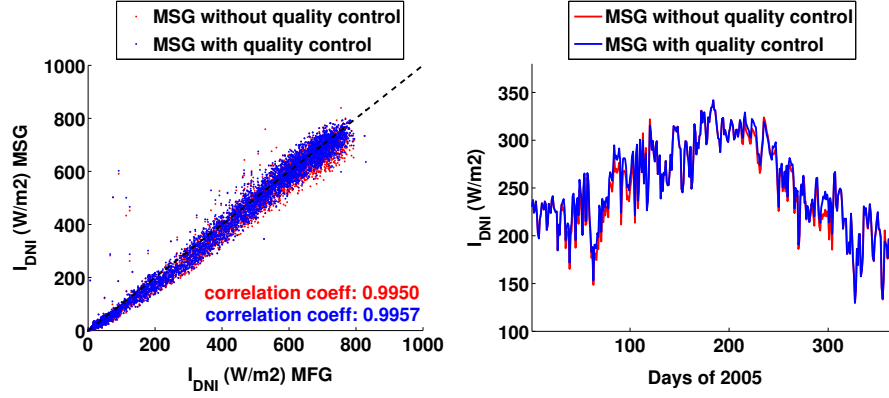
61

Figure 45: Improvement upon quality control of MSG, shown for hourly (left) and daily (right) time-series for North Africa during 2005.

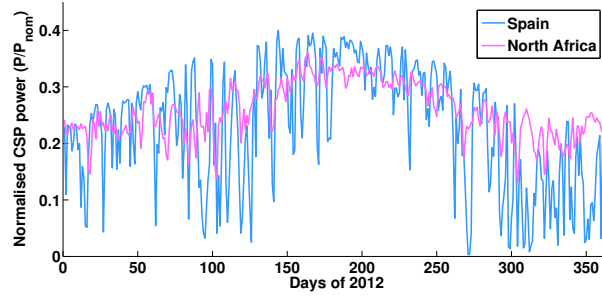### A.3.3. CSP in Spain and North Africa

Figure 46: Daily time series of CSP power normalised to installed capacities during 2012 for Spain and North Africa.

A comparison of daily time series of CSP normalised to the respective installed capacities during 2012 for Spain and North Africa is shown in Fig.46. It shows less fluctuations over North Africa compared to Spain. Fig.46 also shows that in summer, less power is generated in North Africa compared to Spain. This could be a result of using different turbidity modeling schemes in the models for North Africa and Europe. We have used the turbidity from [4] for Europe while for Sahara turbidity is modelled with [18]. The enhanced effects of aerosols from the Sahara desert requires a more selective and sensitive aerosol treatment in the model. The presence of this desert also diminishes the cloud formation and hence North Africa shows a less fluctuating annual course of DNI. This effect is then translated to the CSP power shown in Fig.46. The

62

standard deviation normalised to the respective mean are 0.46 for Spain and 0.19 for North Africa on the daily time series of 2012.
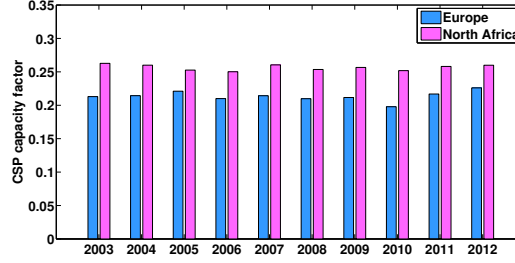

Figure 47: Inter-annual variation of CSP capacity factor for Europe and North Africa.

		normalised standard deviation	annual production (TWh)	standard deviation (GW)
2003	Europe	0.81	166.2	23.4
	North Africa	0.90	204.5	26.1
2004	Europe	0.81	167.7	23.4
	North Africa	0.89	203.5	25.9
2005	Europe	0.83	172.6	23.7
	North Africa	0.88	197.1	25.6
2006	Europe	0.81	163.9	23.0
	North Africa	0.88	194.1	25.4
2007	Europe	0.82	167.2	23.4
	North Africa	0.88	202.7	26.2
2008	Europe	0.81	164.2	23.2
	North Africa	0.88	198.4	25.7
2009	Europe	0.81	165.2	23.3
	North Africa	0.89	200.3	25.8
2010	Europe	0.79	154.4	22.4
	North Africa	0.88	196.5	25.5
2011	Europe	0.81	169.3	23.8
	North Africa	0.88	201.4	26.0
2012	Europe	0.82	176.9	24.4
	North Africa	0.88	203.4	26.2

Table 11: Statistical measures to compare CSP production and variability between Europe and North Africa (standard deviation normalised to mean power, gross annual production for 81GW installed capacity for both Europe and North Africa & standard deviation of hourly time series).

Fig.47 and table11 summarise the inter-annual variability of CSP for Europe and North Africa. Fig.47 reveals that although we assumed same installed capacity of CSP for Europe and North Africa, the later by virtue of its abundant resources has higher capacity factor for all simulated years. The annual capacity factor for Europe appears around 0.20 while for North Africa, it is around 0.25.

References

[1] Arbeitsgruppe Erneuerbare Energien-Statistik (AGEE-Stat). Zeitreihen zur entwicklung der erneuerbaren energien in deutschland. Technical report, Februar 2016.

[2] S. Becker, R.A. Rodriguez, G.B. Andresen, S. Schramm, and M. Greiner. Transmission grid extensions during the build-up of a fully renewable pan-european electricity supply. *Energy*, 64(0):404 – 418, 2014.

[3] Hans Georg Beyer, Jethro Bethke, Anja Drews, Detlev Heinemann, Elke Lorenz, Gerd Heilscher, and Stefan Bofinger. Identification of a general model for the mpp performance of pv-modules for the application in a procedure for the performance check of grid connectedsystems. 19th E. PV. Solar Energy Conference, Paris, 2004.

[4] B. Bourges. *Yearly variations of the Linke turbidity factor, Climatic Data Handbook of Europe.* Kluwer Academic Publishers, Dordrecht, 1992.

[5] D. Cano, J.M. Monget, M. Albuisson, H. Guillard, N. Regas, and L. Wald. A method for the determination of the global solar radiation from meteorological satellite data. *Solar Energy*, 37(1):31 – 39, 1986.

[6] DP Dee, SM Uppala, AJ Simmons, Paul Berrisford, P Poli, S Kobayashi, U Andrae, MA Balmaseda, G Balsamo, P Bauer, et al. The era-interim reanalysis: Configuration and performance of the data assimilation system. *Quarterly Journal of the Royal Meteorological Society*, 137(656):553–597, 2011.

[7] H.G. Beyer et al. Mesor management and exploitation of solar resource knowledge, version-2, sixth framework programme, contract no: 038665. Technical report, August 2009.

[8] M. Fuersch et al. Roadmap 2050 - a closer look. Technical report, EWI, Energynautics, October 2011.

[9] Sven Teske et al. energy [r]evolution - a sustainable eu 27 energy outlook. Technical report, EREC, October 2012.

[10] Dominik Heide, Lueder von Bremen, Martin Greiner, Clemens Hoffmann, Markus Speckmann, and Stefan Bofinger. Seasonal optimal mix of wind and solar power in a future, highly renewable europe. *Renewable Energy*, 35(11):2483 – 2489, 2010.

[11] Thomas Huld, Marcel Šúri, and Ewan D. Dunlop. Comparison of potential solar electricity output from fixed-inclined and two-axis tracking photovoltaic modules in europe. *Progress in Photovoltaics: Research and Applications*, 16(1):47–59, 2008.

[12] Pierre Ineichen. Long term satellite hourly, daily and monthly global, beam and diffuse irradiance validation. interannual variability analysis. Technical report, University of Geneva, December 2013.

[13] D. Kearney and H. Price. Recent advances in parabolic trough solar power plant technology. 2004.

[14] T.M. Klucher. Evaluation of models to predict insolation on tilted surfaces. *Solar Energy*, 23(2):111–114, 1979.

[15] Elke Lorenz, Thomas Scheidsteger, Johannes Hurka, Detlev Heinemann, and Christian Kurz. Regional pv power prediction for improved grid integration. *Progress in Photovoltaics: Research and Applications*, 19(7):757–771, 2011.

[16] R.W. Mueller, K.F. Dagestad, P. Ineichen, M. Schroedter-Homscheidt, S. Cros, D. Dumortier, R. Kuhlemann, J.A. Olseth, G. Piernavieja, C. Reise, L. Wald, and D. Heinemann. Rethinking satellite-based solar irradiance modelling: The {SOLIS} clear-sky module. *Remote Sensing of Environment*, 91(2):160 – 174, 2004.

[17] B. Pfluger, F. Sensfuß, G. Schubert, and J. Leisentritt. Tangible ways towards climate protection in the European Union (EU long-term scenarios 2050). Technical report, Karlsruhe, September 2011.

[18] J. Remund. Aerosol optical depth and linke turbidity climatology, description for final report of iea shc task 36. Technical report, Meteotest Bern, 2009.

[19] Michele M Rienecker, Max J Suarez, Ronald Gelaro, Ricardo Todling, Julio Bacmeister, Emily Liu, Michael G Bosilovich, Siegfried D Schubert, Lawrence Takacs, Gi-Kong Kim, et al. Merra: Nasa's modern-era retrospective analysis for research and applications. *Journal of Climate*, 24(14):3624–3648, 2011.

[20] H. Schmidt and D.U. Sauer. Wechselrichter wirkungsgrade. *Sonnenenergie*, 4:43–47, 1996.

[21] Dr. Franz Trieb. Concentrating solar power for the mediterranean region, final report. Technical report, German Aerospace Center (DLR), April 2005.

[22] M.J. Wagner and P. Gilman. Technical manual for the sam physical trough model. Technical report, NREL/TP-5500-51825, 1617 Cole Boulevard Golden, Colorado 80401, June 2011.

[23] Wikipedia. List of solar thermal power stations — Wikipedia, the free encyclopedia, 2015. [Online; accessed 19-July-2015].

[24] Y. Zhang and S.J. Smith. Long-term modeling of solar energy: analysis of concentrating solar power (csp) and pv technologies. Technical report, Pacific Northwest, National Laboratory, August 2008.